J Mater Sci (2011) 46:2009–2017
DOI 10.1007/s10853-010-5197-6

Evolution of the microstructure and mechanical properties of eutectic $Fe_{30}Ni_{20}Mn_{35}Al_{15}$

Yifeng Liao · Ian Baker

Received: 12 September 2010 / Accepted: 13 December 2010 / Published online: 7 January 2011

Abstract The microstructure of the eutectic alloy $Fe_{30}Ni_{20}Mn_{35}Al_{15}$ (in at.%) was modified by cooling at different rates from 1623 K, i.e., above the eutectic temperature. The lamellar spacing decreased with increasing cooling rate, and in water-quenched specimens lamellae widths of ~100 nm were obtained. The orientation relationship between the fcc and B2 lamellae was found to be sensitive to the cooling rate. In a drop-cast alloy the Kurdjumov–Sachs orientation relationship dominated, whereas the orientation relationship in an arc-melted alloy with a faster cooling rate was fcc$(\bar{1}12)$//B2(011); fcc$[1\bar{1}1]$//B2 $[1\bar{1}1]$ and fcc$(0\bar{1}1)$//B2(001); fcc$[011]$//B2$[\bar{1}\bar{1}0]$. The hardness increased with microstructural refinement, obeying a Hall–Petch-type relationship. The strength of the alloy decreased significantly above 600 K due to softening of the B2 phase.

Introduction

Good strength and room temperature ductility are two essential components in designing structural alloys. A recently discovered, two-phase alloy with nominal composition of $Fe_{30}Ni_{20}Mn_{35}Al_{15}$ is of interest due to its attractive combination of strength and ductility [1]. In the arc-melted state, the alloy has been shown to be composed of very hard ~200 nm wide B2 lamellae and ductile ~500 nm wide fcc lamellae [1]. Upon straining the B2 phase exhibits little plastic deformation; while the fcc phase deforms by the glide of $\langle 110 \rangle$ dislocations forming dislocation pile-ups at the interphase boundaries [2].

How the lamellar spacing of $Fe_{30}Ni_{20}Mn_{35}Al_{15}$ affects its mechanical properties is, as yet, unknown in this alloy. Liu and Maziasz [3] suggested that, since both the grain size and colony size are much larger than the lamellar size in a lamellar microstructure, based on a dislocation pile-up model, the yield stress should be dependent on the lamellar spacing, as governed by a Hall–Petch-type relationship [4, 5]. The correlation between the lamellar size and the mechanical properties has been extensively studied for duplex TiAl, which consists of γ-TiAl ($L1_0$ structure) and α_2-Ti_3Al (DO_{19} structure) phases [4–6]. The lamellar spacing of TiAl is sensitive to both the Al concentration [7] and the heat treatment [8, 9]. By modifying the microstructure, the Hall–Petch relationship has been shown to be applicable over a wide range of lamellar sizes ranging from 30 to 400 nm in hot-extruded TiAl [3, 8]. In addition to Ti–Al, the strength and ductility of other metals, for instance hypo-eutectoid steel, can be tuned by modifying the lamellar spacing via thermo-mechanical treatments [12].

In this study, the lamellar spacing of the alloy $Fe_{30}Ni_{20}Mn_{35}Al_{15}$ was varied by cooling from above the melting point at different rates. The orientation relationship and hardness are presented as a function of lamellar spacing. In addition, the mechanical behavior of drop-cast was examined at intermediate temperatures.

Experimental

$Fe_{30}Ni_{20}Mn_{35}Al_{15}$ alloys were prepared using different casting conditions. First, elemental (>99.8% purity) Fe, Ni,

Y. Liao · I. Baker (✉)
Thayer School of Engineering, Dartmouth College,
8000 Cummings Hall, Hanover, NH 03755, USA
e-mail: Ian.Baker@dartmouth.edu

Present Address:
Y. Liao
Department of Materials Science and Engineering,
Northwestern University, Evanston, IL 60208, USA

Mn, and Al pieces were arc-melted under flowing argon. The melted buttons were cooled in a water-chilled copper crucible. Details have been presented elsewhere [1]. Second, a $Fe_{30}Ni_{20}Mn_{35}Al_{15}$ rod of 25.4 mm (D) × 152.4 mm (L) was drop-cast under an argon atmosphere. The melt was cooled in an alumina crucible and the material was used as a master ingot. A thin piece ~50 mg of the as-drop-cast material was heated up twice in a Perkin Elmer DTA to 1773 K at a heating rate of 20 K/min under an argon atmosphere in order to determine the temperatures of any phase transformations.

Refinement of the lamellar spacing was achieved by heating the alloy in an alumina crucible under argon to 1623 K, which is above the melting point determined from the DTA measurements, holding for 30 min and then either cooling to 1373 K at 10 K/min followed by quenching into water, or quenching directly into water. Material with a coarser microstructure was produced by melting a mixture of elemental pieces at 1873 K in an alumina crucible under argon and directionally solidifying the melt at 18 mm/h in a Bridgman furnace. The end of the crucible was cooled by a water-chilled copper rod in order to produce a high temperature gradient.

Specimens of the above materials were mounted in phenolic resin and polished to a mirror finish using 0.3 μm alumina powder. Vickers hardness values were measured using a Leitz MINIload tester with a load of 1.96 N (200 g). A FEI XL30 field emission gun (FEG) scanning electron microscope (SEM) equipped with energy dispersive spectroscopy (EDS) and operated at 15 kV was used for surface examination. The microstructure was examined in detail using a Tecnai F20 FEG transmission electron microscope (TEM) equipped with an EDS and operated at 200 kV. TEM specimens of the alloys with different heat treatments were prepared as follows: 3 mm diameter discs were produced from the alloys by using electro-discharge machining; they were ground to ~200 μm thick and jet polished in a solution of 30% nitric acid and 10% butoxyethanol in methanol using a Struers Tenupol 5 at 253 K at a voltage of 9 V and a current of 70 mA.

In order to investigate the elevated-temperature mechanical behavior, 3 × 3 × 8 mm specimens of the drop-cast materials were heated to 300–1000 K and compressed at an initial strain rate of 5×10^{-4} s^{-1} using an MTS. Tests were stopped at ~6% strain and specimens were quenched into water. Specimens strained at 300, 600, and 900 K were examined in the TEM.

Results

Phase transformations

The heat flow curves of the two DTA scans between 1350 and 1575 K are compared in Fig. 1. No peak was found

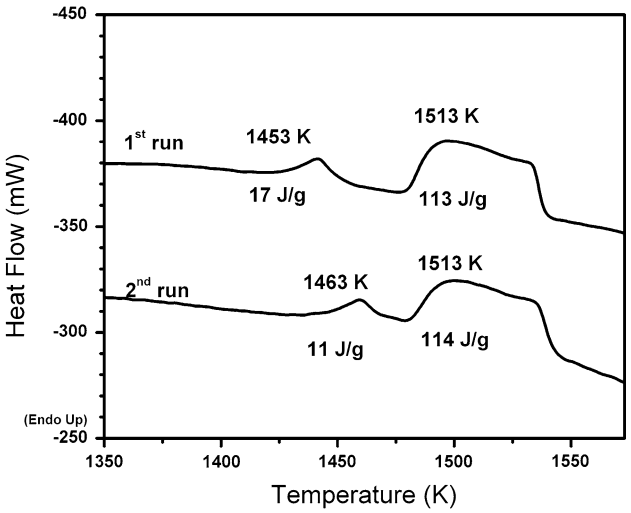

Fig. 1 DTA curves of $Fe_{30}Ni_{20}Mn_{35}Al_{15}$ heated at 20 K/min. Two peaks were observed between 1350 and 1550 K. The peak at ~1453 K possibly is due to disordering from the B2 to the bcc structure, while the broad peak starting at ~1513 K was due to melting

either below 973 K or above 1550 K in the DTA curves. An endothermic peak occurred at ~1453 K in the first run, followed by a broad endothermic peak starting at ~1513 K. The first reaction has an enthalpy of ~17 J/g, and is possibly related to the disordering of the B2 phase. (The unit J/g rather than J/mol is used because the exact mole fractions of the two phases are unknown.) For comparison, disordering of B2 structured Fe_2MnAl occurs at 1305 K, with an associated enthalpy of 34 J/g [10]. This value is twice that of $Fe_{30}Ni_{20}Mn_{35}Al_{15}$. Given the fact that the B2 phase has a volume fraction of ~47% in $Fe_{30}Ni_{20}Mn_{35}Al_{15}$ [1], the enthalpy of disordering of the B2 phase is comparable to that of Fe_2MnAl. This peak shifted to ~1463 K and had an enthalpy of ~11 J/g in the second scan, possibly because the B2 phase was less ordered after the first scan.

The second peak spanning 1513–1545 K in the first scan was due to melting. Integrating the area under the peak gave an enthalpy of ~113 J/g. For comparison, Fe_2MnAl melts at 1677 K with an enthalpy of 166 J/g [10]. A peak occurred at the same temperature, with a nearly identical enthalpy (~114 J/g), in the second scan.

Orientation relationships

Figure 2a shows a TEM image of the drop-cast $Fe_{30}Ni_{20}Mn_{35}Al_{15}$. The lamellae widths were ~200 and ~500 nm for the B2 (dark region) and fcc phase (light region), respectively. A few dislocations were present in the fcc lamellae. The orientation relationship in the drop-cast $Fe_{30}Ni_{20}Mn_{35}Al_{15}$ was determined for four specimens. Figure 2b shows superimposed selected area diffraction

(SAD) patterns from neighboring B2 and fcc lamellae. The B2 phase was tilted to [111] whereas the adjacent fcc lamella was at [011]. As illustrated in Fig. 2b, B2[01$\bar{1}$] and fcc[11$\bar{1}$] were parallel to each other. The orientation relationship was therefore determined to be fcc [11$\bar{1}$]//B2[01$\bar{1}$]; fcc [011]//B2 [111], which is the Kurdjumov–Sachs relationship. The relatively slow cooling rate may have allowed atoms to arrange in such a way that the most-close-packed planes of the B2 and fcc phases are coplanar, forming the Kurdjumov–Sachs orientation relationship.

Figure 3a shows a bright-field TEM micrograph of the arc-melted alloy with lamellae a few hundred nanometers wide, which is similar to the drop-cast material. The dark and light regions represent the B2 and fcc phases, respectively. Two kinds of orientation relationships were identified. First, with the B2 lamellae tilted to [011], the neighboring fcc phase was at [$\bar{1}$12], as shown in the superimposed selected area diffraction (SAD) pattern from neighboring B2 and fcc lamellae in Fig. 3b. The [1$\bar{1}$1] directions in the B2 and fcc phases are parallel to each other. The orientation relationship is therefore concluded to be fcc($\bar{1}$12)//B2(011); fcc[1$\bar{1}$1]//B2[1$\bar{1}$1]. Two specimens out of four examined had this orientation relationship between the phases. The other two specimens had a different orientation relationship. When the B2 lamellae were tilted to [001], the adjacent fcc lamellae were at [0$\bar{1}$1], Fig. 3c shows the superimposed SAD pattern, in which the fcc [011] is nearly parallel to B2 [$\bar{1}\bar{1}$0]. The orientation relationship in this case is close to fcc(0$\bar{1}$1)//B2 (001); fcc[011]//B2[$\bar{1}\bar{1}$0], which is known as Bain relationship [11]. A similar orientation relationship observed in duplex Fe–Mn–Al–C alloys was postulated to be formed via a reverse Bain distortion [12].

Microstructural modification

SEM and TEM micrographs of $Fe_{30}Ni_{20}Mn_{35}Al_{15}$ produced by cooling from 1623 K under different cooling conditions are shown in Fig. 4. In the directionally

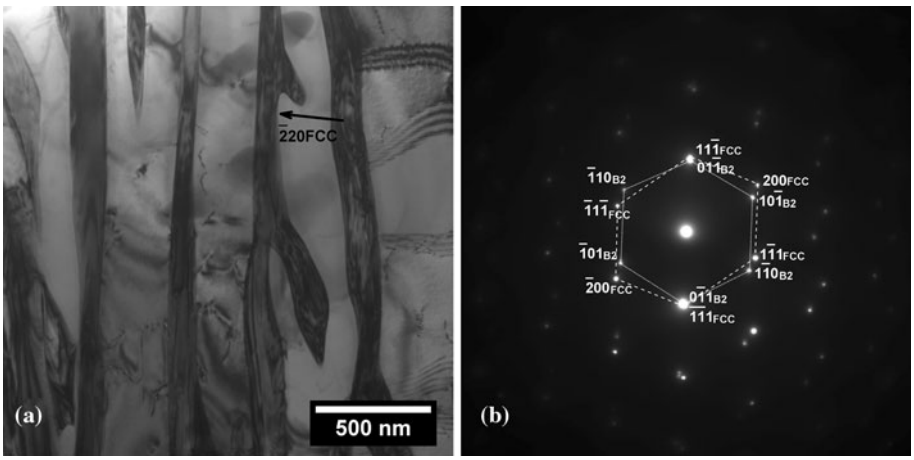

Fig. 2 **a** Bright-field TEM micrograph showing the microstructure of drop-cast $Fe_{30}Ni_{20}Mn_{35}Al_{15}$. **b** Superimposed electron diffraction patterns from the B2 and fcc phases at the B2 [111] zone axis. The fcc phase was tilted to the [011] zone axis. The two phases had a Kurdjumov–Sachs orientation relationship

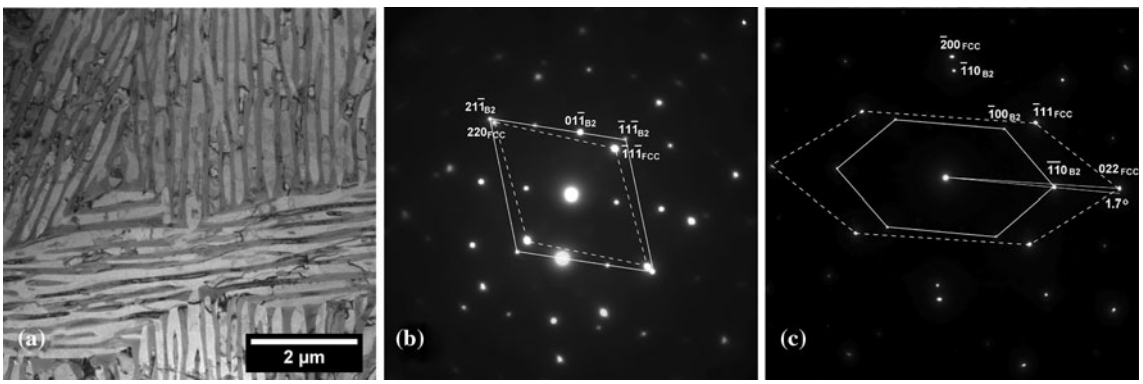

Fig. 3 **a** Bright-field TEM micrograph showing fine fcc (*light region*) and B2 lamellae (*dark region*) in a specimen produced using arc-melting. Two orientation relationships were found in four specimens. **b** Superimposed SAD patterns from the two phases, in which a few B2 and fcc reflection spots are highlighted by the *solid* and *dashed lines*, respectively. B2[1$\bar{1}$1] was aligned with fcc[1$\bar{1}$1], showing fcc($\bar{1}$12)//B2(011); fcc[1$\bar{1}$1]//B2[1$\bar{1}$1] orientation relationship. **c** B2[$\bar{1}\bar{1}$0] was nearly aligned with fcc [011], showing a fcc(0$\bar{1}$1)//B2(001); fcc[011]//B2[$\bar{1}\bar{1}$0] orientation relationship

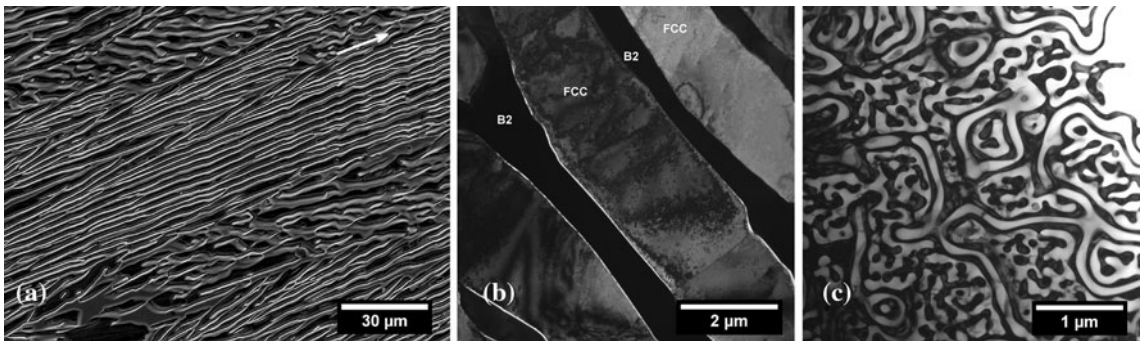

Fig. 4 **a** SEM micrograph of directionally solidified $Fe_{30}Ni_{20}Mn_{35}Al_{15}$. The growth direction is *arrowed*. The B2 lamellae show bright contrast. **b** TEM micrograph of the specimen cooled at 10 K/m and **c** TEM micrograph of the specimen quenched into water from 1623 K. The B2 (*dark*) and fcc (*bright*) lamellae were ~100 nm wide and enclosed within each other

solidified specimen, the lamellae were well-aligned along the growth direction, which is arrowed in the SEM micrograph in Fig. 4a. The B2 lamellae (bright region) and fcc lamellae (light region) were 3–6 μm and ~10 μm wide, respectively.

For the specimen cooled at 10 K/min through the melting point before quenching the B2 lamellae width decreased to 500–700 nm and the fcc lamellae width decreased to ~2 μm, see Fig. 4b. A few dislocations and subgrain boundaries were observed in the fcc lamellae. With further increases in the cooling rate by simply quenching from above the melting point, the lamellar spacing decreased dramatically to 50–70 nm and 80–150 nm for the B2 and fcc phase, respectively, see Fig. 4c. All specimens except that quenched from 1623 K had continuous B2 and fcc lamellae. In contrast, the 1623 K-quenched specimen featured B2 and fcc lamellae enclosing each other.

SAD patterns were obtained for all specimens to confirm that the constituent phases were B2 and fcc phase. No disordering from B2 to bcc or further ordering of the B2 and fcc phases was noted. The chemical compositions measured using EDS in TEM were $Fe_{43}Ni_{12}Mn_{37}Al_8$ for the fcc phase and $Fe_9Ni_{42}Mn_{17}Al_{32}$ for the B2 phase in drop-cast alloy. These are close to the compositions of the constituent phases in an arc-melted specimen previously examined [1]. For all the specimens, the chemical composition of the B2 phase was Ni-rich, whereas the fcc phase was Fe- and Mn-enriched. Thus, the structural and mechanical properties of the individual constituent phases were presumably similar.

The Vickers hardness values showed a clear dependence on the cooling rate from 1623 K. The hardness increased substantially from the as-cast state of 310–380 VPN for the 1623 K-quenched alloy. It decreased to ~230 VPN for the 10 K/s cooled alloy, and decreased further for the directionally solidified alloy to ~210 VPN. The hardnesses and the corresponding B2 and fcc lamellar spacings of $Fe_{30}Ni_{20}Mn_{35}Al_{15}$ produced under different conditions are listed in Table 1.

Table 1 Interlamellar spacing and Vickers hardness of $Fe_{30}Ni_{20}Mn_{35}Al_{15}$ cooled from 1623 K at different rates

	B2 spacing (nm)	fcc spacing (nm)	Hardness (VPN)
D.S. (18 mm/h)	3000–6000	~10000	210
10 K/min	500–700	~2000	230
Drop-cast	~200	~500	310
1623 K-quenched	50–70	80–150	380

Intermediate temperature deformation

Figure 5 shows the stress of the drop cast specimens as a function of temperature. The yield stress slightly decreased from ~750 MPa at 300 K to ~700 MPa at 600 K, then decreased significantly above 600 K and was ~140 MPa at 1000 K. The yield stresses of B2-ordered $Fe_{50}Al_{50}$ [13] and $Ni_{48.9}Al_{51.1}$ [14] are plotted for comparison. $Ni_{48.9}Al_{51.1}$ has a nearly constant yield stress of ~400 MPa below 700 K. The stress decreased rapidly above 700 K and was only 69 MPa at 973 K. The yield stresses of all these alloys are weakly temperature-dependent from room temperature to ~0.45 T_m, and experienced a rapid loss above ~0.45 T_m. Drop-cast $Fe_{30}Ni_{20}Mn_{35}Al_{15}$ work-hardened greatly over the temperature range 300–600 K, whereas above 600–1000 K work-hardening was trivial.

The microstructures of the deformed specimens were subsequently examined in the TEM. Figure 6 shows bright-field micrographs of the specimens deformed at 300, 600, and 900 K. In all cases a large number of dislocations were present in the fcc phase. The B2 phase showed no signs of plastic deformation at 300 K, whereas several dislocations were observed in the specimen strained at 600 K. In the specimen strained at 900 K in Fig. 6c, a number of

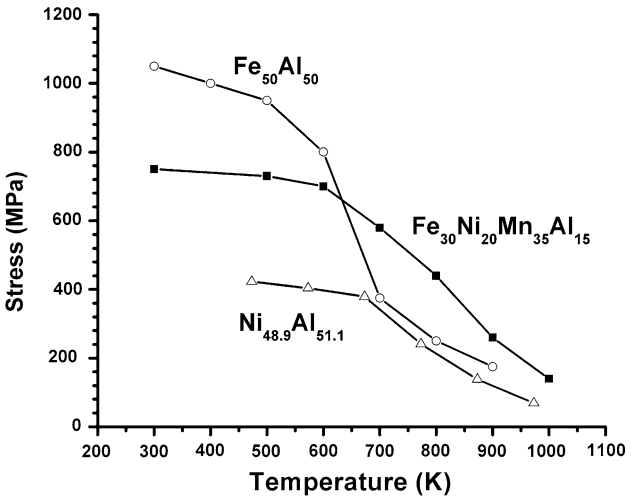

Fig. 5 Stress of drop-cast specimens as a function of temperature. The yield stresses of $Fe_{50}Al_{50}$ [13] and $Ni_{48.9}Al_{51.1}$ [14] are plotted for comparison

dislocations were present in the B2 phase. It is evident that the B2 phase became more deformable above 600 K.

Discussion

Microstructural refinement

The exact cooling rates after drop-casting or arc-melting are unknown. However, arc-melting would produce a faster cooling rate than drop-casting (due to the smaller specimen size and chilled copper hearth of the former) and both are faster than the 10 K/min slow cool: the growth rate of the directionally solidified specimen at 18 mm/h had the slowest cooling rate. The order of the cooling rate is listed as follows in ascending sequence:

$$\text{directional solidification} < 10\,\text{K/min} < \text{drop-cast} < \text{arc-melting} < 1623\,\text{K-quench}$$

The dependence of the interlamellar spacing, λ, in binary eutectic/eutectoid systems on growth rate was examined by Chadwick [15] and Porter and Easterling [16]. Considering diffusion in front of solid interface advancing into an undercooled liquid, the resulting relationship between λ and v is:

$$v\lambda^2 = C \tag{1}$$

where C is a material constant associated with the diffusion coefficient and surface energy. The equation was validated in Al–Zn, Pb–Cd, and Pb–Sn systems [15]. Recently, Bei and George [17] suggested that Eq. 1 also works well in the NiAl–Mo ternary system. Although in the present case the exact growth rate for each specimen is unknown, the trend described by Eq. 1 was observed for $Fe_{30}Ni_{20}Mn_{35}Al_{15}$, i.e., the lamellar spacing decreased with increasing growth rate.

In addition to a reduction in lamellar spacing, the 1673 K-quenched alloy adopted a "Chinese script" morphology. The reason for this discontinuous lamellae morphology is not wholly clear, but is presumably related to both composition and growth rate [18, 19]. In directionally solidified eutectic $Al_2O_3/GdAlO_3$, the discrete 'Chinese script' morphology could only be formed when the volume fraction of Al_2O_3 was between 40 and 60% [18]. The volume fractions of the B2 phase were ~44% for $Fe_{30}Ni_{20}Mn_{35}Al_{15}$ [1], consistent with this observation [18]. Thall and Chalmers [20] reported discontinuous and enclosed Si lamellae in rapidly cooled Al–Si. They suggested that the latent heat and/or thermal conductivity between the Al and Si phases were considerably different. A local temperature difference in the liquid was produced and, as a consequence, the Al phase grew faster than the Si

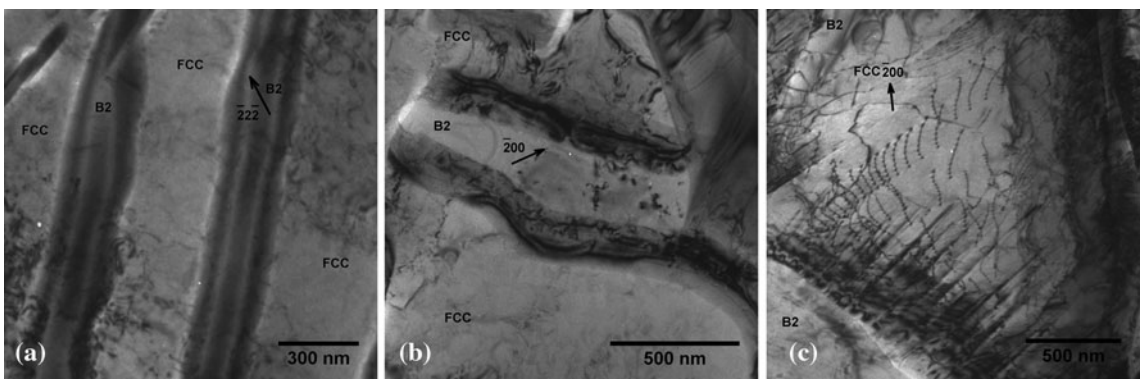

Fig. 6 Bright-field micrographs of drop-cast specimens compressed at **a** 300 K, **b** 600 K, and **c** 900 K. At room temperature the B2 lamellae did not appear to undergo plastic deformation, whereas at 600 and 900 K a few dislocations were observed in the B2 lamellae

phase. The protruding Al lamellae in turn tend to grow over the Si lamellae. This explanation, however, does not account for the morphology in the present study, because the fcc and B2 phases were enclosed by each other. An alternative mechanism was postulated by Croker et al. [19] after directionally solidifying eutectic Bi–Pb_2Bi produced at different growth rate (10^{-4} to 10^{-2} mm/s). The alloy changed from a cellular structure at low growth rate to a discrete structure at high growth rate. They attributed the morphology change to the competition of the heat withdrawal along the longitudinal direction and constitutional supercooling along the lateral direction [19].

As noted earlier, the yield stress of a lamellar structure can generally be described by the Hall–Petch-type relationship [8]:

$$\sigma = \sigma_0 + k\lambda^{-1/2} \tag{2}$$

where σ is yield stress, σ_0 is friction stress, and k is a constant. Equation 2 can also be extended to hardness data. Huang et al. [6] examined the hardness of Nb, B, and W doped Ti–Al with controlled lamellar spacing. The hardness was ~285 VPN when $\lambda = 2.48$ μm and increased to ~310 VPN with $\lambda = 2.07$ μm. Elwazri et al. [21] reported that this relationship also applied to hypereutectoid steel based on 12 measurements with the lamellar spacing ranged from 0.11 to 0.22 μm. However, the use of this equation often leads to a negative friction stress in steels [22]. In order to avoid the non-physical value, modification of Eq. 2 by changing the exponent from −0.5 to −1, has been suggested [22, 23].

For $Fe_{30}Ni_{20}Mn_{35}Al_{15}$, the yield strength of the drop-cast alloy with the finer structure was clearly higher than that of directionally solidified alloy, a tendency also apparent in the Vickers hardness data. As discussed elsewhere [2], plastic deformation took place solely within the fcc phase. It is therefore reasonable to relate the hardness to the fcc lamellae width. The hardness is plotted as function of both $\lambda^{-1/2}$ and λ^{-1} in Fig. 7. Both plots give physically real (positive) values for the intercept, and the residual sum of square fitting with $\lambda^{-1/2}$ is 318, whereas the residual sum of square fitting with λ^{-1} is 1802. Thus, the Hall-Patch relationship with an exponent of −0.5 appears to fit the experimental data better.

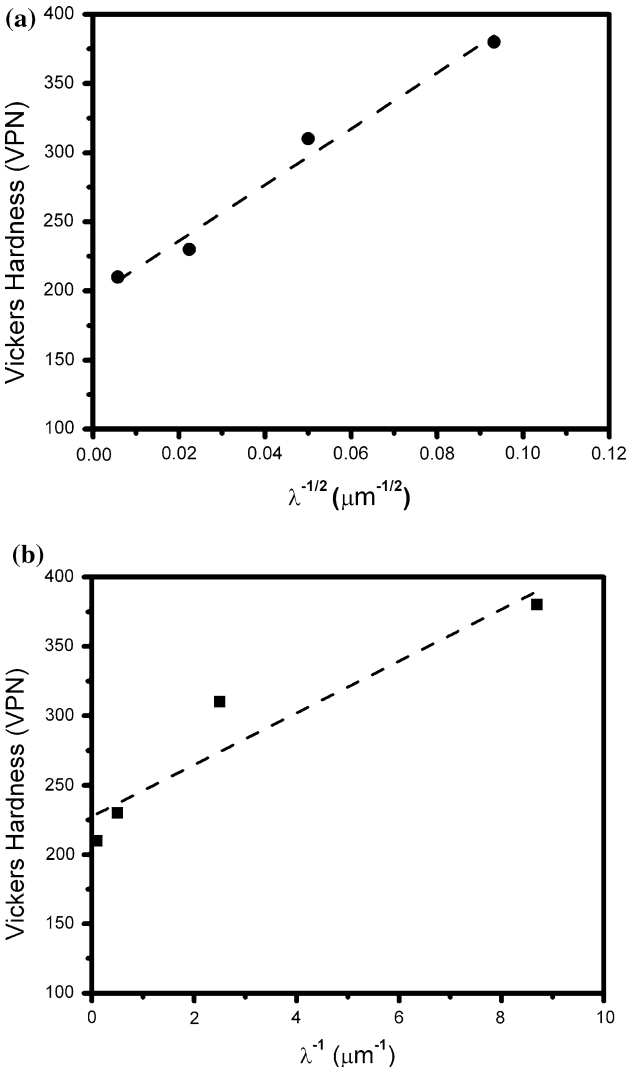

Fig. 7 Vickers hardness as a function of **a** $\lambda^{-1/2}$ and **b** λ^{-1}, where λ is the fcc lamellar spacing

Orientation relationships

While the Kurdjumov–Sachs orientation relationship is frequently observed in many bcc–fcc compounds, the two orientation relationships observed in the arc-melted specimens are less understood. The superimposed stereographic projections of these two relationships are plotted in Fig. 8. The traces of B2 $[10\bar{1}]$, $[\bar{1}\bar{1}0]$, $[121]$, $[1\bar{1}\bar{2}]$ are shown in Fig. 8a and the traces of B2 $[111]$, $[11\bar{1}]$, $[\bar{1}1\bar{1}]$, $[\bar{1}11]$ are shown in Fig. 8b. The {111} close-packed-planes of the fcc phase are not aligned with the {110} close-packed plane of the B2 phase for either of the two orientation relationships. The misorientation between the phases is larger than those of Kurdjumov–Sachs and Nishiyama–Wassermann orientation relationships commonly seen in fcc–bcc compounds [24]. The relatively faster cooling rate during the arc-melting may be the reason for the large mismatch between the orientations of the phases.

It is of interest to understand the impact of the orientation relationship change on the mechanical behavior. Consider a group of dislocations in the fcc phase piling up at the interface, as illustrated in Fig. 9 (adapted from Smith and Barnby [25]). The local shear stress in the B2 phase induced by the dislocation pile-up is given by [25, 26]:

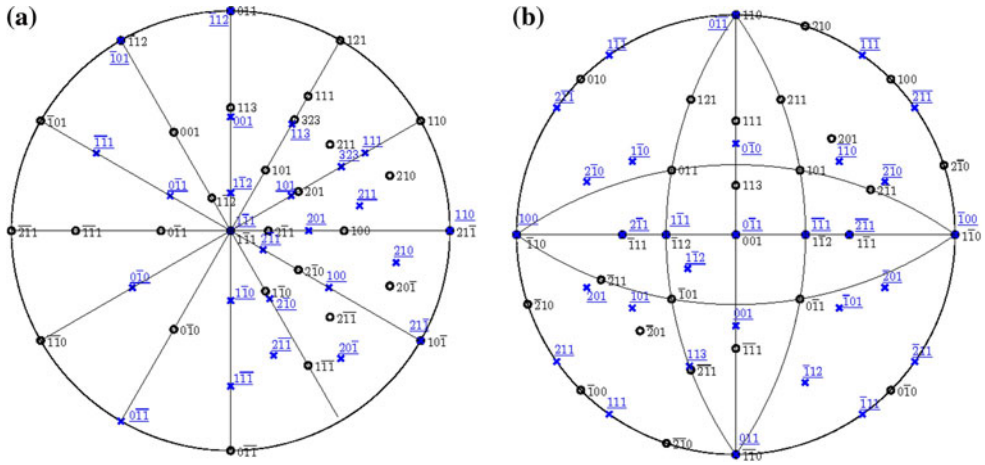

Fig. 8 Superimposed stereographic projections of the B2 and fcc phases in arc-melted $Fe_{30}Ni_{20}Mn_{35}Al_{15}$. **a** fcc($\bar{1}12$)//B2(011) and fcc[$1\bar{1}1$]//B2[$1\bar{1}1$] and **b** fcc($0\bar{1}1$)//B2(001); fcc[011]//B2[$\bar{1}\bar{1}0$]. The poles marked by cross with *underlined* indices represent the ones in the fcc phase, while those in the B2 phase are marked by *open circles*

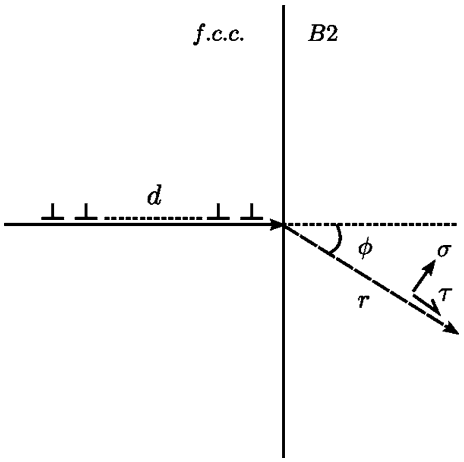

Fig. 9 Schematic of the local stresses in the B2 phase caused by dislocation pile-up at the phase boundary within the fcc phase. Adapted from Smith and Barnby [25]

$$\tau = \sigma_{\mathrm{E}}\left(\frac{d}{r}\right)^{0.5}\frac{2\cos(3\phi/2)+\sin(\phi)\sin(\phi/2)}{2} \qquad (3)$$

where d is the length of pile-up group, r is the distance from the leading dislocation to the point of interest in the B2 phase, ϕ is the angle between the incoming and outgoing slip vectors on either side of the interface. The effective stress σ_{E} is the net shear stress exerted on a dislocation in the fcc structure, which is equal to the applied shear stress on the slip plane (σ_{a}) subtracted by the friction stress (σ_{f}), i.e., $\sigma_{\mathrm{E}} = \sigma_{\mathrm{a}} - \sigma_{\mathrm{f}}$.

To create a dislocation in the B2 phase, τ has to exceed the critical resolved shear stress on the slip plane. From Eq. 1, τ depends on the angle ϕ given by the geometric factor $F = \frac{2\cos(3\phi/2)+\sin(\phi)\sin(\phi/2)}{2}$. At $\phi = 0°$, i.e., the situation for the Kurdjumov–Sachs relationship, the geometric factor has a maximum value of 1.0. τ decreases with increasing ϕ. As the slip vectors in the fcc phases ($\langle 110\rangle$) and in the B2 phase ($\langle 111\rangle$) are known, the angles between the slip vectors can be calculated. Table 2 lists the angles between all $\langle 110\rangle$ slip vectors in the fcc phase and the nearest $\langle 111\rangle$ slip vectors in the B2 phase for the two orientation relationships found in this study. The geometric factors F are also calculated. It is evident that the smallest angle between the slip vectors in the fcc and B2 phases is for the case when fcc($\bar{1}12$)//B2(011); fcc[$1\bar{1}1$]//B2[$1\bar{1}1$] and is $\sim$19°. The corresponding geometry factor F is $\sim$ 0.91. For the orientation relationship fcc($0\bar{1}1$)//B2 (001); fcc[011]//B2[$\bar{1}\bar{1}0$], the smallest angle is $\sim$30°, when the F is $\sim$0.77. It has been suggested, based on experimental observations, that ϕ should be smaller than 15° to allow direct slip transfer between the phases [27, 28]. Thus, the orientation relationship in arc-melted $Fe_{30}Ni_{20}Mn_{35}Al_{15}$ is one of the factors that hinder direct slip transfer from the fcc phase to the B2 phase. This is in sharp contrast to the frequent dislocation transmission between the fcc and B2 phases in $Ni_{50}Al_{20}Fe_{30}$ [31, 32], where the slip transfer is favored by the large geometric factor of 1.0 [29].

Temperature dependence of the mechanical properties

The microstructure of the drop-cast alloy was stable at temperatures up to 1000 K: TEM images of specimens strained at up to 1000 K, showed no evidence of lamellar coarsening. This stability below the melting point of $Fe_{30}Ni_{20}Mn_{35}Al_{15}$ is similar to observations on some other eutectic alloys including Al–Cu and Al–Ni [30]. Ramanujan et al. [4] also reported that boron-modified Ti–47Al showed little change in microstructure after ageing at

Table 2 Angles between the slip vectors of the fcc and B2 phases for the two orientation relationships observed in arc-melted specimens

fcc slip vectors	fcc($\bar{1}12$)//B2(011) fcc[$1\bar{1}1$]//B2[$1\bar{1}1$]			fcc($0\bar{1}1$)// B2 (001) fcc[011]//B2[$\bar{1}\bar{1}0$]		
	Nearest B2 slip vectors	Angles (°)	F	Nearest B2 slip vectors	Angles (°)	F
[110]	[$11\bar{1}$]	19	0.91	[$1\bar{1}1$]	30	0.77
[101]	[$1\bar{1}1$]	34	0.71	[$\bar{1}11$]	30	0.77
[011]	[111]	19	0.91	[111], [$11\bar{1}$]	35	0.70
[$1\bar{1}0$]	[$1\bar{1}1$]	34	0.71	[$\bar{1}11$]	30	0.77
[$10\bar{1}$]	[$\bar{1}11$]	19	0.91	[$1\bar{1}1$]	30	0.77
[$01\bar{1}$]	[$1\bar{1}1$]	34	0.71	All ⟨111⟩	55	0.32

The F factors are calculated

1073 K for 168 h. Fuchs examined the effect of homogenizing temperature on the Ti–48Al–2Nb–2Cr and found that at 1473 K no significant change occurred [31]. The resistance to coarsening and spheroidizing of the constituent phases makes eutectic/eutectoid alloys potentially valuable in high temperature applications [30].

The yield stress was roughly constant from room temperature to 600 K. In this stage, the B2 lamellae are hard and act as obstacles to dislocation motion. The yield stress decreased rapidly between 600 and 1000 K, a feature observed in many B2 ordered intermetallic compounds above 0.45 T_m [32]. Based on the TEM observations the lamellar spacing and orientation relationship was quite stable in this temperature range. The B2 phases experienced a brittle–ductile transition and showed some plasticity. The reduced dislocation impediment capability by the B2 lamellae is presumably one of the reasons for the substantial drop of the yield stress above 600 K.

Conclusions

The lamellar structure of the $Fe_{30}Ni_{20}Mn_{35}Al_{15}$ two-phase B2/fcc eutectic alloy can be modified by cooling from above the eutectic point at different rates. With increased cooling rate, the lamellar size decreased from a few microns in a directionally solidified alloy to ~100 nm in a quenched alloy. Correspondingly, the hardness increased, obeying a Hall–Petch-type relationship with the width of the fcc lamellae. While a drop-cast alloy had a Kurdjumov–Sachs orientation relationship, the orientation relationship changed to fcc($\bar{1}12$)//B2(011); fcc[$1\bar{1}1$]//B2[$1\bar{1}1$] or fcc($0\bar{1}1$)//B2(001); fcc[011]//B2[$\bar{1}\bar{1}0$] in the specimens produced by arc-melting which had a faster cooling rate. The alloy experiences a significant decrease in yield strength above 600 K presumably due to the softening of the B2 phase.

Acknowledgements The authors are grateful to Dr. Easo George and Dr. Hongbin Bei of the Oak Ridge National Laboratory, Oak Ridge, TN., for providing the drop-cast ingots. This research was supported by National Science Foundation Grant DMR 0552380 and DMR 0905229. Any opinions, findings, and conclusions or recommendations expressed in this material are those of the author(s) and do not necessarily reflect the views of the National Science Foundation or the U.S. Government.

References

1. Liao YF, Baker I (2008) Mater Charact 59(11):1546
2. Liao Y, Baker I (2010) Mater Sci Eng A (submitted)
3. Liu CT, Maziasz PJ (1998) Intermetallics 6(7–8):653
4. Ramanujan RV, Maziasz PJ, Liu CT (1996) Acta Mater 44(7): 2611
5. Maruyama K, Yamada N, Sato H (2001) Mater Sci Eng A 319: 360
6. Huang L, Liaw PK, Liu CT (2007) Metall Mater Trans A 38A(13): 2290
7. Umakoshi Y, Nakano T, Yamane T (1992) Mater Sci Eng A 152(1–2):81
8. Liu CT, Schneibel JH, Maziasz PJ, Wright JL, Easton DS (1996) Intermetallics 4(6):429
9. Umeda H, Kishida K, Inui H, Yamaguchi M (1997) Mater Sci Eng A 240:336
10. Wittmann M, Baker I, Munroe PR (2004) Philos Mag 84(29): 3169
11. Bain EC, Dunkirk NY (1924) Trans Am Inst Min Metall Petrol Eng 70:22
12. Chen SK, Wan CM, Byrne JG (1990) Scr Metall Mater 24(11): 2139
13. Baker I, Gaydosh DJ (1987) Mater Sci Eng 96:147
14. Ball A, Smallman RE (1966) Acta Metall Mater 14(10):1349
15. Chadwick GA (1963) Prog Mater Sci 12(2):99
16. Porter DA, Easterling KE (1992) Phase transformation in metals and alloys. CRC Press, New York
17. Bei H, George EP (2005) Acta Mater 53(1):69
18. Kaiden H, Durbin SD, Yoshikawa A, Lee JH, Sugiyama K, Fukuda T (2002) J Alloy Compd 336(1–2):259
19. Croker MN, Mcparlan M, Baragar D, Smith RW (1975) J Cryst Growth 29(1):85
20. Thall BM, Chalmers B (1950) J I Met 77(1):79
21. Elwazri AM, Wanjara P, Yue S (2005) Mater Sci Eng A 404(1–2):91

22. Dollar M, Bernstein IM, Thompson AW (1988) Acta Metall Mater 36(2):311
23. Ray KK, Mondal D (1991) Acta Metall Mater 39(10):2201
24. He YL, Godet S, Jonas JJ (2005) Acta Mater 53(4):1179
25. Smith E, Barnby JT (1967) Metal Sci J 1:56
26. Stroh AN (1954) Proc R Soc Lond A 223:404
27. Misra A, Gibala R (1999) Metall Mater Trans A 30(4):991
28. Shen Z, Wagoner RH, Clark WAT (1988) Acta Metall Mater 36(12):3231
29. Misra A, Gibala R (2000) Intermetallics 8(9–11):1025
30. Hertzberg RW (1967) Composite materials formed by the directional solidification of eutectic alloys. Addison-Wesley, London
31. Fuchs GE (1997) Metall Mater Trans A 28(12):2543
32. Baker I (1995) Mater Sci Eng A 193:1